

24 **that in Campi Flegrei and other similar magmatic systems, magma recharge may both**
25 **increase repose times and reduce the likelihood of eruption.**

26 Volcanic gases (principally H₂O and CO₂) dissolved in silicate melts exert a first-order
27 control on the eruptive behaviour of many volcanoes¹⁻³. Vapour saturation in magmas is
28 reached due to depressurisation during ascent^{1,4} or through ‘second boiling’ during
29 progressive crystallisation^{5,6}. Once saturation is achieved, growth of vapour bubbles during
30 continued crystallisation^{5,6} or magma chamber replenishment^{7,8} will continue to pressurise
31 the magma reservoir, and may eventually trigger an eruption. Determining both pre-eruptive
32 volatile concentrations and the timing of volatile saturation is therefore critical to our
33 understanding of magmatic processes and eruption dynamics. Although many models assume
34 that saturation occurs early in magmatic evolution (e.g. refs 1, 9-11), it is often not known
35 whether this is the case; or whether, instead, melts can remain undersaturated on long time-
36 scales during crustal storage and differentiation. To address this, we need to constrain the
37 variations in dissolved magmatic volatile contents through time, during the build up to an
38 explosive eruption. An ability to do this would be particularly helpful for hazard assessment
39 of dormant systems where the build-up to eruption has not previously been monitored, as past
40 eruptions may provide clues to the future behaviour of the system.

41 Apatite, Ca₅(PO₄)₃(F,Cl,OH), is a common accessory phase in most igneous rocks, and takes
42 all major magmatic volatiles (OH, C, S, Cl, F) into its crystal structure. It has recently been
43 used to elucidate the volatile contents of silicate melts in terrestrial^{12,13} and extra-terrestrial¹⁴⁻
44 ¹⁶ environments. Apatite offers a number of important benefits for the determination of pre-
45 eruptive magmatic volatile contents over the widely-used ‘melt inclusion’ approach. In
46 particular, apatites are less susceptible to post-entrapment volatile leakage, or to modification
47 by processes such as post-entrapment crystallisation or bubble growth that frequently inhibit
48 the use of melt inclusions¹⁷. Here, we present analyses of both apatite and melt inclusions,

49 hosted within different phenocryst phases (clinopyroxene and biotite) that were trapped and
 50 isolated from the melt at different times through the crystallisation history of an evolving
 51 magma. We also analysed apatite microphenocrysts that were in contact with the melt and
 52 able to rehomogenise until shortly before eruption; and matrix glasses, which quenched
 53 during eruption. In combination with thermodynamic modelling, these “texturally
 54 constrained” hydrous phases provide a time-series of magmatic volatile evolution (Fig.1) in
 55 the build-up to the phonolitic Astroni 1 eruption, which occurred at 4.3-4.1 ka¹⁸ (sample
 56 description in Supplementary Materials). This event represents the onset of activity from the
 57 vent that produced the most recent prolonged phase of explosive volcanism at Campi Flegrei,
 58 one of the most hazardous volcanoes in Europe¹⁸. Our approach is distinct from previous
 59 studies, which have assessed apatite growth zoning¹³ or texturally unconstrained analyses¹².
 60 Although we focus on a single event, our approach can be applied widely to determine the
 61 temporal evolution of pre-eruptive volatiles in other volcanic systems.

62 **Volatile variations in apatite and hydrous glasses**

63 The volatile composition of apatite is related to that of its host liquid by a set of exchange
 64 reactions between F, Cl and OH, e.g.:

$$65 \quad K_{(P,T)} = \frac{f_{H_2O}^l}{f_{HF}^l} \cdot \frac{X_F^{Ap}}{X_{OH}^{Ap}} \quad (1)$$

66 where exchange coefficients, K , are constant at a given pressure (P) and temperature (T)¹², f
 67 is fugacity, X is mole fraction and superscripts l and Ap denote the liquid and apatite phases
 68 respectively. In this study, we measured F, Cl and OH directly using secondary ion mass
 69 spectrometry and electron microprobe analysis (see Supplementary Methods). As S diffusion
 70 in apatite is inhibited by a coupled substitution¹⁹, equilibrium is not maintained on short
 71 timescales and it is not considered further. Apatite compositions from Astroni 1 show a

negative correlation between X_F and X_{OH} and a weaker negative correlation between X_{Cl} and X_{OH} (where X_F , X_{Cl} and X_{OH} are mole fraction F, Cl and OH respectively; Supplementary Table 1), demonstrating this exchange of components within the crystal volatile site. Some crystals are slightly non-stoichiometric, within the range reported in other studies²⁰. We focus primarily on mole fraction ratios as these are related to liquid composition, pressure and temperature through equations such as equation (1). Data show a positive correlation between X_{Cl}/X_{OH} and X_F/X_{OH} (Fig. 2a), with one low- X_{Cl} , high- X_F outlier. In general, X_F/X_{Cl} is constant within error, except in the outlier which has high X_F/X_{Cl} (Fig. 2b). Clinopyroxene-hosted apatite inclusions extend to higher $X_{halogen}/X_{OH}$ ratios than biotite-hosted apatite inclusions. Both clinopyroxene- and biotite-hosted inclusions extend to higher $X_{halogen}/X_{OH}$ ratios than apatite microphenocrysts, which were in contact with the melt until the time of eruption. The overall $X_{halogen}/X_{OH}$ trend appears to be linear, suggesting that there was no significant relative change in F or Cl compatibility during apatite crystallisation.

Melt inclusions are typically phonolitic, with an average $Na/(Na+K)$ of 0.44 and $Al_2O_3/(CaO+Na_2O+K_2O)$ of 0.87, similar to Vesuvian melt compositions²¹. MgO and FeO concentrations are <0.78 wt% and <4.20 wt%, respectively (Supplementary Table 2). The F and Cl contents of clinopyroxene- and biotite-hosted melt inclusions correlate negatively with MgO (Fig. 3a,b), reflecting halogen incompatibility in the silicate melt during fractionation. Water is constant within error in clinopyroxene-hosted melt inclusions (~2 wt%), but is highly variable in biotite-hosted inclusions (1.3-4.5 wt%), with no correlation between melt inclusion H_2O and MgO (Fig. 3d). All melt inclusions contain very low CO_2 contents, typically <250 ppm (Supplementary Table 2), similar to concentrations observed in other Campi Flegrei magmas^{10,22}.

Matrix glasses have similar MgO contents to the most evolved melt inclusions. Fluorine and Cl contents are similar to those of biotite-hosted melt inclusions and the most evolved

97 clinopyroxene-hosted inclusions (Fig. 3a-c). However, matrix glasses have low H₂O contents
98 relative to both clinopyroxene- and biotite-hosted melt inclusions, typically <1 wt% (Fig. 3d).

99 **Modelling fractionation and volatile saturation**

100 We modelled magma evolution in the Campi Flegrei system using the Rhyolite-MELTS
101 thermodynamic software²³, following the approach of refs 24-26 (details in Supplementary
102 Discussion). Since major and trace element trends between different eruptions of Campi
103 Flegrei can be related by fractional crystallisation of a single parental magma²⁷, we use the
104 most primitive olivine-hosted melt inclusion reported from the last 15 ka (Mi1-C1-o5-M1 of
105 ref. 28) as the starting composition in our models. Models were run over the pressure range
106 50-300 MPa, at $fO_2=QFM+1$ and with liquidus H₂O concentrations (L_{H_2O}) of 2-3 wt%, in
107 order to simulate the entire range of conditions identified in previous phase equilibria and
108 petrological studies as best reproducing the stable phase assemblages observed in Campi
109 Flegrei eruptions²⁴⁻²⁶. Since Rhyolite-MELTS uses a pure-H₂O solubility model that is not
110 appropriate for alkali melts (see Supplementary Discussion), we repressed fluid exsolution
111 within Rhyolite-MELTS and instead used recent experimental data as a guide to volatile
112 saturation in the Campi Flegrei system (Fig. 4).

113 The model results confirm the crystallisation sequence: olivine (~1330 °C) + clinopyroxene
114 (~1080 °C) + apatite (~1020 °C) + biotite (~910 °C) + K-feldspar (~790 °C) at 150 MPa,
115 $L_{H_2O}=3$ wt% (Fig. 4). This matches the observed phase assemblage in the Astroni 1 erupted
116 products (see Supplementary Materials), except that olivine is absent in natural samples and
117 fluorite occurs as a microphenocryst phase. Fluorite saturation is constrained to low
118 temperatures by its absence as inclusions within other phases. Within the modelled range,
119 L_{H_2O} has no effect on the order of crystallisation, but clinopyroxene and apatite both arrive on
120 the liquidus at slightly higher temperatures at lower L_{H_2O} conditions ($\Delta T \sim 20$ °C and ~ 30 °C

respectively). During fractionation, modelled melt MgO contents decrease from ~3.8 wt% at clinopyroxene-in to ~0.2 wt% at K-feldspar-in; dissolved H₂O contents increase from 3.7 wt% to 6.2 wt% over the same interval. Pressure has little effect on the profile of the modelled down-temperature MgO and H₂O evolution of the system before volatile saturation is achieved but would change L_{H₂O} if volatile saturation occurred before olivine-in (Fig. 4).

Magma storage pressures can be constrained independently using geophysical estimates of the current depth of the Campi Flegrei magma reservoir. On the basis of seismic reflection data, the main melt zone beneath the current Campi Flegrei caldera is at ~7-7.5 km^{29,30}, with possible ephemeral sills and intrusions extending to ~3 km^{30,31}. This equates to pressures of 170-180 MPa for the main crystallisation region, assuming a melt density of 2440 kgm⁻³. The H₂O solubility of phonolitic melts is >7.5 wt% at 900-950 °C, 200 MPa²¹, falling to ~6.33 wt% H₂O at 870 °C, 150 MPa and <3 wt% H₂O at <50 MPa³². Based on these experimental data, H₂O saturation in our model runs is achieved at 760-775 °C at 200 MPa and 780-800 °C at 150 MPa, within the range L_{H₂O}= 2-3 wt% (Fig. 4). In both cases this is significantly later than apatite-in (Fig. 4).

Progressive temporal trends in melt volatile contents

The modelled crystallisation sequence provides the context for us to interpret progressive changes in melt and apatite volatile compositions, from clinopyroxene-hosted melt or apatite inclusions, to biotite-hosted inclusions, to microphenocrysts and matrix glasses.

Apatite-liquid exchange coefficients (equation 1) have been constrained experimentally for the system apatite-fluid as a function of pressure and temperature (ref. 12 and references therein). At constant melt volatile composition, decreasing temperature causes a strong increase in apatite X_{halogen}/X_{OH} ratios (Fig. 2a). However, the pressure dependence is small and almost exclusively affects X_{Cl}/X_{OH} (e.g. ref. 12). The trend of decreasing X_{Cl}/X_{OH} and

X_F/X_{OH} during magmatic evolution, revealed by our dataset, is therefore inconsistent with changing K due to cooling or depressurisation (Fig. 2a; see Supplementary Discussion for model details). Although magma mixing may cause temporary heating, interpretations involving significant long-term heating or pressurisation are not geologically realistic during prolonged magmatic fractionation, which is required to produce the Astroni 1 phenocryst assemblage, from clinopyroxene to feldspar (Fig. 4). It follows that the observed trend in apatite compositions reflects a progressive change in the melt volatile composition through time, during magma evolution.

Within the limits of analytical precision, melt inclusions show that melt halogen concentrations increased throughout the course of magma evolution (Fig. 3a-c). Assuming that K_D (equation 1) does not vary significantly with evolving melt composition, the decreasing apatite $X_{halogen}/X_{OH}$ ratios (Fig. 2) must therefore reflect a comparative increase in dissolved melt H_2O contents during crystallisation: i.e. H_2O -undersaturated behaviour. This concurs with our Rhyolite-MELTS modelling. When compared with phonolite solubility experiments^{21,32}, models predicts late, low-temperature H_2O saturation, with melt H_2O concentrations increasing throughout magmatic evolution, at pressures consistent with independent estimates of magma storage depths from current geophysical observations at Campi Flegrei (i.e. $P > 150$ MPa; Fig. 4).

The trends in apatite compositional evolution observed from Astroni 1 can be reproduced using models based on volatile-undersaturated fractionation³³, assuming moderate incompatibility for F, Cl and H_2O during crystallisation of apatite and biotite from the melt (insets Fig. 2; Supplementary Discussion). The effect of biotite precipitation on apatite compositional evolution is minor³³, while the effect of late-stage vapour saturation on the compositional evolution of apatite is orders of magnitude more significant³³. This is because vapour-melt Cl partition coefficients in H_2O -saturated phonolites are >1 (e.g. 9 at 150 MPa;

ref. 34), whereas F is retained within the silicate liquid²¹. The effect of this is to increase the F/Cl ratio in the melt. Therefore, after vapour saturation apatite will move towards a F-Cl binary composition, progressing towards end-member fluorapatite (case 2 of ref. 33; insets Fig. 2). As this trend is not observed in our dataset (see Fig. 2), we infer that the system remained volatile-undersaturated while the apatite microphenocrysts were in equilibrium with the melt.

If the melt inclusions were trapped in the presence of an immiscible hydrosaline brine, we would expect to see constant melt Cl instead of the observed negative correlation between Cl and MgO (Fig. 3a). Experimental data have shown that in the presence of a vapour phase, Cl-solubility in phonolitic magmas is pressure dependent³⁴. The highest Cl concentrations measured in Astroni 1 melt inclusions (>1 wt%) would require extremely low entrapment pressures (<25 MPa) under vapour-saturated conditions³⁴, implying an unrealistically shallow crystallisation depth. Rather, our data are consistent with crystallisation in the absence of a free fluid, in agreement with experimental constraints³⁵.

Melt inclusion halogen concentrations show a negative correlation with MgO (Fig. 3a,b), which is consistent with incompatible behaviour during crystallisation. However, the lack of correlation between H₂O and MgO in melt inclusions (Fig. 3d) cannot be reconciled either with apatite compositions (Fig. 2) or crystallisation models (Fig. 4). Instead, we suggest that the H₂O contents of melt inclusions have been modified by diffusion after entrapment, whereas halogen concentrations record primary magmatic processes. Hydrogen diffusion through pyroxene is rapid, even at 800 °C (refs 36,37) and is a known cause of post-entrapment modification of melt inclusion volatile contents³⁸. From published H diffusivity data, the H₂O concentrations of clinopyroxene-hosted melt inclusions in the centre of large, mm-scale phenocrysts will be altered on timescales of hours^{36,37}. Thus, short-term stalling or slowing of the magma at shallow depths during ascent, after volatile saturation, provides a

mechanism by which the H₂O contents of melt inclusions with varying MgO concentrations can be reset. No data exist for H diffusivity in biotite, although the strong cleavage would presumably reduce its competency as a melt inclusion host. High H₂O concentrations in some biotite-hosted inclusions (Fig. 3d) suggest that melt H₂O contents could have reached >4.5 wt% during biotite crystallisation. However, biotite-hosted melt inclusions with low H₂O contents, approaching concentrations measured in matrix glasses, have probably leaked. The low H₂O content of matrix glass is consistent with efficient syn-eruptive degassing during magma ascent. Under equilibrium conditions at depth, Cl would partition preferentially into the vapour phase³⁴. However, halogens diffuse significantly more slowly than H₂O in silicate melts³⁹, inhibiting vapour-melt equilibration and inducing disequilibrium on short timescales during ascent. Thus, degassed matrix glasses may retain similar Cl concentrations to evolved melt inclusions (Fig. 3). At low pressure, vapour-melt Cl partition coefficients approach unity³⁴ and Cl will remain in the melt once it has ascended to shallow crustal levels.

Timescales of volatile undersaturation

If the magma achieved volatile saturation prior to eruption this should result in disequilibrium between the melt and pre-existing apatite microphenocrysts. However, apatite volatile data show no evidence for partial re-equilibration towards strongly Cl-poor, F-rich (volatile-saturated) compositions as predicted by the model of ref. 33 (Fig. 2), even within 16 µm of the crystal rims (Supplementary Fig. 1). We can use diffusion constraints to estimate the maximum equilibration time between volatile saturation and eruption. Experimental data⁴⁰ suggest that at 800 °C, 1 GPa, the characteristic timescale for halogen diffusion over distances of ~16 µm is ~10 days. At 1 atm this time would be ~3 yr. Our observations therefore suggest that the maximum time before eruption in which volatile saturation could have been achieved in Astroni 1 is on the order days to a few years. Hence, the magma

chamber remained persistently H₂O-undersaturated until only very shortly before eruption. Similarly, the lack of evidence for syn-eruptive volatile loss from apatite microphenocrysts is due to the diffusive re-equilibration time far exceeding realistic eruptive timescales.

Pre-eruptive volatile undersaturation at Campi Flegrei

In combination, apatite and melt inclusion analysis offers great potential as a forensic petrologic tool, providing new information about the temporal evolution of pre-eruptive volatile contents of volcanic systems. Using this method, we have demonstrated that the Astroni 1 magma chamber remained H₂O-undersaturated until shortly before eruption. This interpretation is consistent with thermodynamic modelling of magma evolution (Fig. 4), and with interpretations of ongoing patterns of degassing and deformation in Campi Flegrei, which can be explained by local volatile saturation at the roof of a largely H₂O-undersaturated magma chamber⁴¹. We observe a measurable decrease in apatite $X_{\text{halogen}}/X_{\text{OH}}$ between biotite-hosted inclusions and microphenocrysts, indicating continued crystallisation and an increase in melt H₂O concentration after biotite-in. Given that H₂O saturation is predicted at only slightly lower temperatures than biotite-in (Fig. 4), but microphenocrysts have not re-equilibrated with a volatile-saturated melt, we suggest that the melt achieved H₂O saturation just before eruption. In Astroni 1, only a small amount of additional crystallisation is required to significantly increase in the abundance of the aqueous vapour phase (Fig. 4), generating overpressures exceeding the fracture criterion and inducing eruption⁵ (Supplementary Fig. 2). We cannot discount that pre-eruptive melt H₂O contents remained below saturation until eruption was initiated by an external trigger; however, in the absence of any evidence for an external trigger, we suggest that progressive concentration of dissolved H₂O in the silicate melt triggered eruption when saturation was eventually achieved.

Because H₂O concentrations increase during crystallisation, we infer that fresh batches of mafic melt arriving from depth would probably be more volatile-undersaturated than the evolved melts within an upper crustal reservoir. Although Astroni 1 shows no evidence of pre-eruptive magma mixing^{18,42}, mingling is reported in other Campi Flegrei eruptions, including later eruptions from the Astroni vent^{11,18,42}. The solubility of H₂O in phonolite is not significantly affected by temperature⁴³, so assuming efficient mixing, pre-eruptive magma replenishment would serve to “dilute” the dissolved volatile content of the silicate melt, driving the system back towards a more strongly undersaturated state. In this case, the repose period between eruptions would be related to both the timescale of upper crustal storage and crystallisation (driving the system towards volatile saturation), and the recharge rate (driving it away). Volatile-undersaturated recharge would require greater crustal deformation than volatile-saturated mixing, to accommodate new melt without exceeding the fracture criterion⁴⁴. Such deformation may be responsible for observed large-scale inter-eruptive bradyseismicity at Campi Flegrei^{45,46}, with recharge events inducing significant magma chamber dilation during repose periods.

Volcanological implications

Our data demonstrate that the sub-volcanic feeding systems for explosive eruptions can remain volatile-undersaturated until late in their evolution. This implies that the depths of magma stalling and storage are not controlled by changes in melt rheology resulting from degassing-induced crystallisation⁴⁷, but instead may be a function of local crustal discontinuities in density or rigidity⁴⁸. Furthermore, melt inclusion H₂O-CO₂ data only give a minimum estimate of crystallisation pressures.

This potential for persistent magmatic volatile undersaturation has significant implications for the monitoring of restless volcanoes. While magma chamber assembly can occur on decadal

timescales⁴⁹, there is a growing number of well-documented examples where observed deformation pulses are not immediately followed by eruption; and others, including the only historic eruption of Campi Flegrei⁴⁵, where explosive eruptions begin with little or no early geodetic ‘warning’^{50,51}. This suggests that the final pre-eruptive ‘priming’ of the system may occur on far shorter timescales than the timescales of assembly; perhaps as short as days to months. Since ground-deformation and seismic evidence for unrest may accompany the long-term processes of subterranean magma recharge and chamber assembly, and not simply pre-eruptive activity, this poses a challenge for agencies engaged in volcano monitoring. This is not a ubiquitous triggering mechanism. However, in persistently volatile-undersaturated systems, the signals of pre-eruptive activity may instead be those accompanying volatile saturation, such as leakage of magmatic volatiles out of the reservoir and into the surrounding edifice, or hydrothermal system. At the surface, this would lead to a higher magmatic component to fumarolic gases. Successful monitoring of these systems will therefore demand high time-resolution chemical and isotopic analysis of fluid and gas emissions⁴⁶.

Methods Summary

A representative bulk sample of the Astroni 1 pyroclastic deposit was obtained from within the Campi Flegrei caldera in Naples, Italy. Clinopyroxene and biotite phenocrysts were picked and apatite microphenocrysts were separated using magnetic and heavy liquid separation techniques. All samples were mounted in epoxy resin, carbon coated and mapped using a FEI Quanta 650 FEG-scanning electron microscope (SEM) operating with a 20 kV and ~7 nA beam.

Major and trace elements were measured in apatites and hydrous glasses using a JEOL 8600 wavelength-dispersive electron-microprobe (EPMA). Apatite analyses were collected with a 10 nA, 15 kV, defocused (5 µm diameter) beam and reduced halogen count times to limit the

291 potential for halogen migration during irradiation. Samples and standards were carbon coated
292 together before analysis to ensure constant light element X-ray attenuation. Glass analyses
293 were collected using a 6 nA, 15 kV, defocussed (10 μm diameter) beam and short Na count
294 times, to reduce alkali loss during irradiation. Secondary standards were analysed to check
295 the accuracy and reproducibility of results (Supplementary Table 3). Samples were re-
296 polished after SEM and EPMA analysis, to remove any potential compositional modification
297 resulting from electron-beam exposure.

298 Samples were gold coated and analysed for light-element isotopes using a Cameca ims-4f
299 ion-microprobe, operating with a 10 keV $^{16}\text{O}^+$ primary ion beam. For apatite, spot analyses
300 were made using a 5 nA beam for most analyses, which was reduced to 2.5 nA for smaller
301 inclusions. To reduce any surface contamination, samples were pre-sputtered for ≥ 3 min
302 before analysis, with a raster of 10-15 μm^2 . Melt inclusion volatiles were measured in two
303 separate analyses. In the first analysis, H_2O , F and light-elements were measured using a 4
304 nA primary ion beam, with a ≥ 3 min pre-sputter over a 10 μm^2 area. The second analysis, for
305 CO_2 measurement, was made in the same spot, using 4 nA beam and ≥ 2 min pre-sputter over
306 a 15 μm^2 area. A field aperture was applied during melt inclusion analysis to further reduce
307 contamination from the crater edges, limiting the measured secondary ions to the central ~ 8 -
308 10 μm in the first analyses and ~ 20 μm in the second analyses.

309 Working curves for apatite H_2O , F, and Cl concentrations were produced using a range of
310 natural and synthetic apatite standards, as ^1H , ^{19}F or ^{35}Cl , normalised to ^{44}Ca (Supplementary
311 Fig. 3). Equivalent working curves for glass H_2O and CO_2 concentrations were produced as
312 ^1H or ^{12}C , normalised to ^{30}Si (Supplementary Figs. 4,5). Fluorine and other trace elements
313 were calibrated in glass analyses against NIST SRM610, with ^{44}Ca as an internal standard.
314 Full method details are available in the Supplementary Information.

315 **References**

- 316 1 Roggensack, K., Hervig, R. L., McKnight, S. B. & Williams, S. N. Explosive Basaltic
317 Volcanism from Cerro Negro Volcano: Influence of Volatiles on Eruptive Style.
318 *Science* **277**, 1639-1642 (1997).
- 319 2 Wilson, L. Relationships between pressure, volatile content and ejecta velocity in
320 three types of volcanic explosion. *J. Volc.and Geotherm. Res.* **8**, 297-313 (1980).
- 321 3 Huppert, H. E. & Woods, A. W. The role of volatiles in magma chamber dynamics.
322 *Nature* **420**, 493-495 (2002).
- 323 4 Woods, A. W. & Koyaguchi, T. Transitions between explosive and effusive eruptions
324 of silicic magmas. *Nature* **370**, 641-644 (1994).
- 325 5 Tait, S., Jaupart, C. & Vergnolle, S. Pressure, gas content and eruption periodicity of
326 a shallow, crystallising magma chamber. *Earth Planet. Sci. Lett.* **92**, 107-123 (1989).
- 327 6 Blake, S. Volatile oversaturation during the evolution of silicic magma chambers as
328 an eruption trigger. *J. Geophys. Res.* **89**, 8237-8244 (1984).
- 329 7 Folch, A. & Martí, J. The generation of overpressure in felsic magma chambers by
330 replenishment. *Earth Planet. Sci. Lett.* **163**, 301-314 (1998).
- 331 8 Sparks, S. R., Sigurdsson, H. & Wilson, L. Magma mixing: a mechanism for
332 triggering acid explosive eruptions. *Nature* **267**, 315-318 (1977).
- 333 9 Humphreys, M., Blundy, J. & Sparks, R. Shallow-level decompression crystallisation
334 and deep magma supply at Shiveluch Volcano. *Contrib. Mineral. Petrol.* **155**, 45-61
335 (2008).
- 336 10 Arienzo, I., Moretti, R., Civetta, L., Orsi, G. & Papale, P. The feeding system of
337 Agnano–Monte Spina eruption (Campi Flegrei, Italy): dragging the past into present
338 activity and future scenarios. *Chem. Geol.* **270**, 135-147 (2010).

- 339 11 Isaia, R., D'Antonio, M., Dell'Erba, F., Di Vito, M. & Orsi, G. The Astroni volcano:
340 the only example of closely spaced eruptions in the same vent area during the recent
341 history of the Campi Flegrei caldera (Italy). *J. Volc. Geotherm. Res.* **133**, 171-192
342 (2004).
- 343 12 Piccoli, P. & Candela, P. Apatite in felsic rocks; a model for the estimation of initial
344 halogen concentrations in the Bishop Tuff (Long Valley) and Tuolumne Intrusive
345 Suite (Sierra Nevada Batholith) magmas. *Am. J. Sci.* **294**, 92-135 (1994).
- 346 13 Boyce, J. W. & Hervig, R. L. Magmatic degassing histories from apatite volatile
347 stratigraphy. *Geology* **36**, 63-66 (2008).
- 348 14 McCubbin, F. M. & Nekvasil, H. Maskelynite-hosted apatite in the Chassigny
349 meteorite: Insights into late-stage magmatic volatile evolution in martian magmas.
350 *Am. Min.* **93**, 676-684 (2008).
- 351 15 McCubbin, F. M. *et al.* Fluorine and chlorine abundances in lunar apatite:
352 Implications for heterogeneous distributions of magmatic volatiles in the lunar
353 interior. *Geochim. Cosmochim. Acta* **75**, 5073-5093 (2011).
- 354 16 Boyce, J., Tomlinson, S., McCubbin, F., Greenwood, J. & Treiman, A. The lunar
355 apatite paradox. *Science* **344**, 400-402 (2014).
- 356 17 Lowenstern, J. B. *Applications of silicate-melt inclusions to the study of magmatic*
357 *volatiles* (Magmas, fluids, and ore deposits, Min. Soc. Canada, Québec, 1995).
- 358 18 Smith, V., Isaia, R. & Pearce, N. Tephrostratigraphy and glass compositions of post-
359 15 kyr Campi Flegrei eruptions: implications for eruption history and
360 chronostratigraphic markers. *Quat. Sci. Rev.* **30**, 3638-3660 (2011).
- 361 19 Peng, G., Luhr, J. F. & McGee, J. J. Factors controlling sulfur concentrations in
362 volcanic apatite. *Am. Min.* **82**, 1210-1224 (1997).

363 20 Nadeau, S. L., Epstein, S. & Stolper, E. Hydrogen and carbon abundances and
364 isotopic ratios in apatite from alkaline intrusive complexes, with a focus on
365 carbonatites. *Geochim. Cosmochim. Acta* **63**, 1837-1851 (1999).

366 21 Webster, J., Goldoff, B., Sintoni, M., Shimizu, N. & De Vivo, B. C–O–H–Cl–S–F
367 volatile solubilities, partitioning, and mixing in phonolitic–trachytic melts and
368 aqueous–carbonic vapor±saline liquid at 200 MPa. *J. Petrol.* **55**, 2217-2248 (2014).

369 22 Marianelli, P., Sbrana, A. & Proto, M. Magma chamber of the Campi Flegrei
370 supervolcano at the time of eruption of the Campanian Ignimbrite. *Geology* **34**, 937-
371 940 (2006).

372 23 Gualda, G. A., Ghiorso, M. S., Lemons, R. V. & Carley, T. L. Rhyolite-MELTS: a
373 modified calibration of MELTS optimized for silica-rich, fluid-bearing magmatic
374 systems. *J. Petrol.* **53**, 875-890 (2012).

375 24 Fowler, S. J., Spera, F. J., Bohrson, W. A., Belkin, H. E. & De Vivo, B. Phase
376 equilibria constraints on the chemical and physical evolution of the Campanian
377 Ignimbrite. *J. Petrol.* **48**, 459-493 (2007).

378 25 Cannatelli, C. Understanding magma evolution at Campi Flegrei (Campania, Italy)
379 volcanic complex using melt inclusions and phase equilibria. *Mineral. Petrol.* **104**,
380 29-42 (2012).

381 26 Bohrson, W. A. *et al. Petrogenesis of the Campanian ignimbrite: implications for*
382 *crystal-melt separation and open-system processes from major and trace elements*
383 *and Th isotopic data* (Developments in Volcanology, Elsevier, New York, 2006).

384 27 Civetta, L., Carluccio, E., Innocenti, F., Sbrana, A. & Taddeucci, G. Magma chamber
385 evolution under the Phlegraean Fields during the last 10 ka: trace element and isotop
386 data. *Eur. J. Mineral.* **3**, 415-428 (1991).

387 28 Cannatelli, C. *et al.* Geochemistry of melt inclusions from the Fondo Riccio and
388 Minopoli 1 eruptions at Campi Flegrei (Italy). *Chem. Geol.* **237**, 418-432 (2007).

389 29 Zollo, A. *et al.* Seismic reflections reveal a massive melt layer feeding Campi Flegrei
390 caldera. *Geophys. Res. Lett.* **35** L12306 (2008).

391 30 De Siena, L., Del Pezzo, E. & Bianco, F. Seismic attenuation imaging of Campi
392 Flegrei: Evidence of gas reservoirs, hydrothermal basins, and feeding systems. *J.*
393 *Geophys. Res.* **115** B09312 (2010).

394 31 Woo, J. Y. & Kilburn, C. R. Intrusion and deformation at Campi Flegrei, southern
395 Italy: sills, dikes, and regional extension. *J. Geophys. Res.* **115** B12210 (2010).

396 32 Carroll, M. R. & Blank, J. G. The solubility of H₂O in phonolitic melts. *Am. Min.* **82**,
397 549-556 (1997).

398 33 Candela, P. A. Toward a thermodynamic model for the halogens in magmatic
399 systems: an application to melt-vapor-apatite equilibria. *Chem. Geol.* **57**, 289-301
400 (1986).

401 34 Signorelli, S. & Carroll, M. Solubility and fluid-melt partitioning of Cl in hydrous
402 phonolitic melts. *Geochim. Cosmochim. Acta* **64**, 2851-2862 (2000).

403 35 Webster, J. D. & De Vivo, B. Experimental and modeled solubilities of chlorine in
404 aluminosilicate melts, consequences of magma evolution, and implications for
405 exsolution of hydrous chloride melt at Mt. Somma-Vesuvius. *Am. Min.* **87**, 1046-1061
406 (2002).

407 36 Woods, S. C., Mackwell, S. & Dyar, D. Hydrogen in diopside: diffusion profiles. *Am.*
408 *Min.* **85**, 480-487 (2000).

409 37 Ferriss, E., Plank, T., Walker, D. & Nettles, M. The whole-block approach to
410 measuring hydrogen diffusivity in nominally anhydrous minerals. *Am. Min.* **100**, 837-
411 851 (2015).

412 38 Danyushevsky, L. V., McNeill, A. W. & Sobolev, A. V. Experimental and
413 petrological studies of melt inclusions in phenocrysts from mantle-derived magmas:
414 an overview of techniques, advantages and complications. *Chem. Geol.* **183**, 5-24
415 (2002).

416 39 Baker, D. R., Freda, C., Brooker, R. A. & Scarlato, P. Volatile diffusion in silicate
417 melts and its effects on melt inclusions. *Ann. Geophys.* **48**, 699-717 (2005).

418 40 Brenan, J. Kinetics of fluorine, chlorine and hydroxyl exchange in fluorapatite. *Chem.*
419 *Geol.* **110**, 195-210 (1993).

420 41 Bodnar, R. J. *et al.* Quantitative model for magma degassing and ground deformation
421 (bradyseism) at Campi Flegrei, Italy: Implications for future eruptions. *Geology* **35**,
422 791-794 (2007).

423 42 Tonarini, S., D'Antonio, M., Di Vito, M. A., Orsi, G. & Carandente, A. Geochemical
424 and B–Sr–Nd isotopic evidence for mingling and mixing processes in the magmatic
425 system that fed the Astroni volcano (4.1–3.8 ka) within the Campi Flegrei caldera
426 (southern Italy). *Lithos* **107**, 135-151 (2009).

427 43 Schmidt, B. C. & Behrens, H. Water solubility in phonolite melts: Influence of melt
428 composition and temperature. *Chem. Geol.* **256**, 259-268 (2008).

429 44 Blake, S. Volcanism and the dynamics of open magma chambers. *Nature* **289**, 783-
430 785 (1981).

431 45 Guidoboni, E. & Ciuccarelli, C. The Campi Flegrei caldera: historical revision and
432 new data on seismic crises, bradyseisms, the Monte Nuovo eruption and ensuing
433 earthquakes (twelfth century 1582 AD). *Bull. Volc.* **73**, 655-677 (2011).

434 46 Chiodini, G. *et al.* Evidence of thermal-driven processes triggering the 2005–2014
435 unrest at Campi Flegrei caldera. *Earth Planet. Sci. Lett.* **414**, 58-67 (2015).

- 436 47 Annen, C., Blundy, J. & Sparks, R. The genesis of intermediate and silicic magmas in
437 deep crustal hot zones. *J. Pet.* **47**, 505-539 (2006).
- 438 48 Chaussard, E. & Amelung, F. Regional controls on magma ascent and storage in
439 volcanic arcs. *Geochem., Geophys., Geosyst.* **15**, 1407-1418 (2014).
- 440 49 Druitt, T., Costa, F., Deloule, E., Dungan, M. & Scaillet, B. Decadal to monthly
441 timescales of magma transfer and reservoir growth at a caldera volcano. *Nature* **482**,
442 77-80 (2012).
- 443 50 Parks, M. M. *et al.* Evolution of Santorini Volcano dominated by episodic and rapid
444 fluxes of melt from depth. *Nat. Geosci.* **5**, 749-754 (2012).
- 445 51 Biggs, J. *et al.* Global link between deformation and volcanic eruption quantified by
446 satellite imagery. *Nat Commun.* **5**, 3471 (2014).

447 **Acknowledgements**

448 This research was funded by a NERC studentship NE/K500811/01 awarded to M.J.S. and a
449 NERC Edinburgh Ion Microprobe Facility grant (IMF519/0514). M.C.S.H. was supported by
450 a Royal Society University Research Fellowship. M.C.S.H. and V.C.S. acknowledge funding
451 from NERC grant NE/K003852/1. This work has benefited from discussion with R. Brooker,
452 J. Riker and P. Candela. The review of W. Bohrson significantly improved the manuscript.
453 We are grateful to R. Hinton and N. Charnley for assistance with SIMS and SEM analysis
454 respectively. We also thank D. Harlov for providing synthetic apatite standards for SIMS
455 calibration and R. van Elsas for technical support during mineral separation.

456 **Author Contributions**

457 M.J.S. and M.C.S.H. conceived the project and analytical strategy. V.C.S. and R.I. collected
458 samples, M.J.S. and V.C.S. made the EPMA and SIMS analyses and M.J.S. and M.C.S.H.

performed the modelling. M.J.S. analysed the data and wrote the first draft of the manuscript, which was revised by all authors.

Competing financial interests

The authors declare no competing financial interests.

Figure legends

Figure 1 | Textural relationships of different hydrous phases in the Astroni 1 magma and the preservation of a temporally constrained magmatic volatile record. a,b,

Backscattered-electron (BSE) images showing apatite and melt inclusions hosted within (a) a clinopyroxene and (b) a biotite phenocryst. c, BSE image of an apatite microphenocryst, rimmed by silicate glass, demonstrating the potential for diffusive apatite-melt exchange until the matrix was quenched on eruption. d-f, Sketches summarising the model by which hydrous phases obtain and retain the volatile composition of the silicate melt during fractionation. Apatite crystals and melt inclusions are progressively trapped within pyroxene and biotite phenocrysts and are subsequently considered closed to diffusive exchange with the melt (except for H₂O in melt inclusions; see discussion in text). Apatite microphenocrysts continue to grow and equilibrate with the melt on timescales controlled by individual species diffusivities⁴⁰. Volatile saturation occurs before eruption (f). g, The relative timescales over which texturally constrained hydrous phases preserve a record of melt volatile contents. h, Schematic graph showing the hypothetical volatile-undersaturated evolution of H₂O (black line) and halogens (grey line) in a silicate melt during isobaric cooling and crystallisation, followed by H₂O saturation and ascent. The concentration of H₂O in the melt would be buffered during crystallisation if vapour saturation occurred significantly before eruption. After vapour saturation under equilibrium conditions, the F/Cl ratio in the melt will increase. However, equilibration may be kinetically inhibited during rapid ascent, causing halogen

concentrations in the melt to remain approximately constant despite the presence of a vapour phase (see text for details). Vertical lines show the relative timing of mineral precipitation and microphenocryst equilibration. t_1 - t_5 refer to the relative timing of events shown in panel **h**. t_4 represents the time after which apatite microphenocryst compositions are preserved on eruption; before this they are reset by diffusional re-equilibration. t_{eruption} and t_{sat} denote the relative onset of ascent and H_2O saturation, respectively. Scale bars are 250 μm in **a**, 500 μm in **b** and 100 μm in **c**. ap= apatite, cpx= clinopyroxene, bt= biotite, mag= magnetite, MI= melt inclusion, MG= matrix glass.

Figure 2 | The volatile compositions of Astroni 1 apatites. a, Apatite volatile compositions in $X_{\text{F}}/X_{\text{OH}}$ versus $X_{\text{Cl}}/X_{\text{OH}}$ space. Black arrows show the modelled trajectory of apatite compositional evolution with decreasing temperature (1200-700 °C), at a constant melt volatile composition and at pressures of 50 MPa (solid line), 100 MPa (dashed line) and 300 MPa (dotted line). Dark grey arrows show the modelled trajectory of apatite compositional evolution with decreasing pressure (1000-0 MPa), at a constant melt volatile composition and at temperatures of 800 °C (solid line), 1000 °C (dashed line) and 1200 °C (dotted line). This modelling was undertaken using the equations of ref. 12 (see Supplementary Discussion for details). **b**, Apatite volatile compositions in $X_{\text{F}}/X_{\text{Cl}}$ versus $X_{\text{Cl}}/X_{\text{OH}}$ space. Insets show the trajectory of apatite compositions during volatile-undersaturated (solid light grey line) and volatile-saturated (dashed light grey line) crystallisation, calculated using an adaptation of the model in ref. 33 to account for differences in the relative compatibility of volatile species during hydrous mineral precipitation (see Supplementary Discussion for details). Apatite crystallisation begins at the black point, biotite-in is after 40% crystallisation (grey cross) and volatile saturation occurs after 73% crystallisation (black cross). If vapour saturation occurred in Astroni 1, apatites would move to high $X_{\text{Cl}}/X_{\text{OH}}$ ratios, progressing towards fluorapatite end-member

compositions (case 2 of ref. 33) due to the high H₂O solubility²¹ and vapour-melt Cl partition coefficient³⁴. The general measured trend of decreasing $X_{\text{halogen}}/X_{\text{OH}}$ is incongruent with the modelled compositional trend caused by cooling or depressurisation, or with equilibrium with a H₂O-saturated melt. All elements were measured by SIMS. Errors bars represent precision with a 90% confidence interval, as detailed in the Supplementary Methods. Data are distinguished on the basis of phenocryst host and textural association (see legend).

Figure 3 | The volatile contents of Astroni 1 hydrous glasses. a, b, MgO versus Cl and F respectively. c, F versus Cl. d, MgO versus H₂O. MgO and Cl were measured by EPMA. F and H₂O were measured by SIMS. Error bars represent precision with ± 1 s.d (EPMA data) and a 90% confidence interval (SIMS data), as detailed in the Supplementary Methods. Data are distinguished on the basis of their phenocryst host or textural association (see legend).

Figure 4 | Rhyolite-MELTS thermodynamic modelling of the Astroni 1 system. The dashed black line shows total solids and solid lines show modelled phase proportions at 150 MPa and $L_{\text{H}_2\text{O}}=3$ wt%. This is similar to observed phase assemblage in Astroni 1, except that olivine is absent as a phenocryst phase in natural sample (see Supplementary Materials). The light and dark blue dashed lines show the modelled H₂O concentration dissolved in the silicate melt at 150 MPa, $L_{\text{H}_2\text{O}}=2$ wt% and 3 wt% respectively. The blue fields show the range of dissolved H₂O contents modelled for these $L_{\text{H}_2\text{O}}$ concentrations within the pressure range 50-300 MPa. The light and dark orange dashed lines show the modelled MgO concentration of the melt at 150 MPa and $L_{\text{H}_2\text{O}}=2$ wt% and 3 wt% respectively. The orange field shows the range of melt MgO concentrations within the pressure range 50-300 MPa and $L_{\text{H}_2\text{O}}=2-3$ wt%. The dashed red line shows the H₂O concentration at volatile saturation for a low-CO₂ phonolite at 910-944 °C, 200 MPa, based on experiments in ref. 21. The dotted red line shows the saturation H₂O concentration for a CO₂-free phonolite at 870 °C, 150 MPa, based on experiments in ref. 32. The starting composition in this model is melt inclusion

533 Mi1-C1-o5-M1 of ref. 28. Within a realistic pressure and L_{H_2O} range, the Astroni 1 magma
534 chamber is likely to reach H_2O saturation at $T \approx 800$ °C. Ol = olivine (black dots); mag =
535 magnetite (diagonal lines); cpx = clinopyroxene (vertical lines); ap = apatite; Pl= plagioclase
536 (spots); bi = biotite (diagonal lines); Kfs= K-feldspar (horizontal lines).

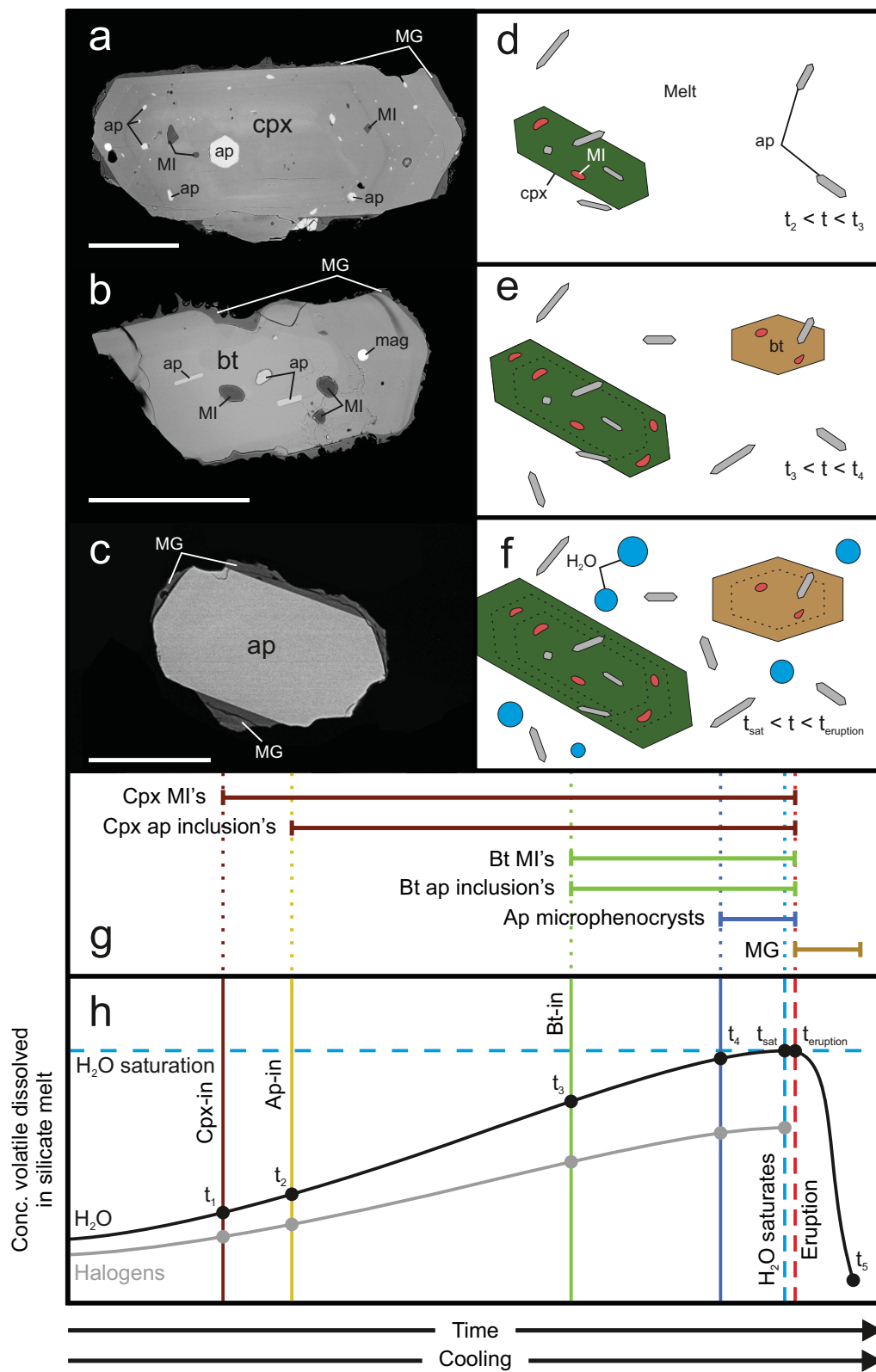


Figure 1

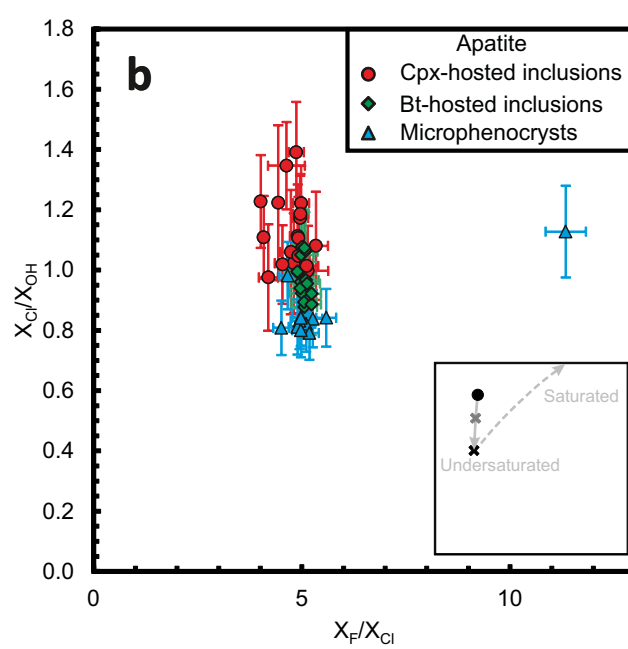
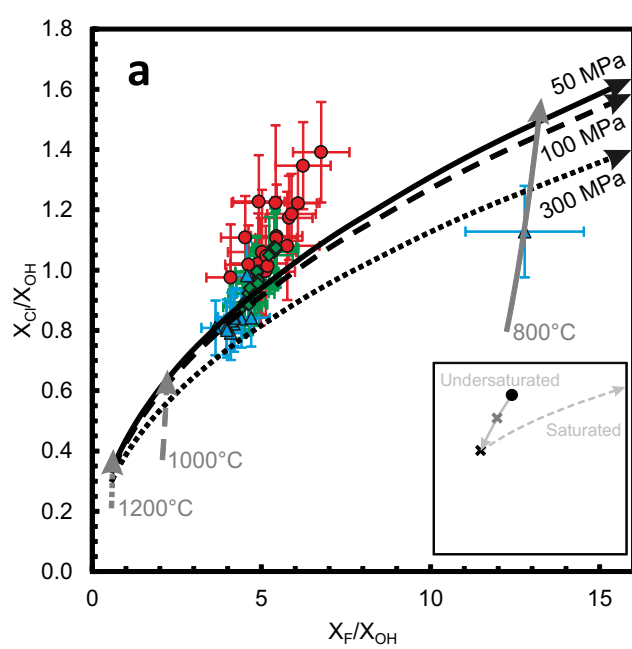


Figure 2

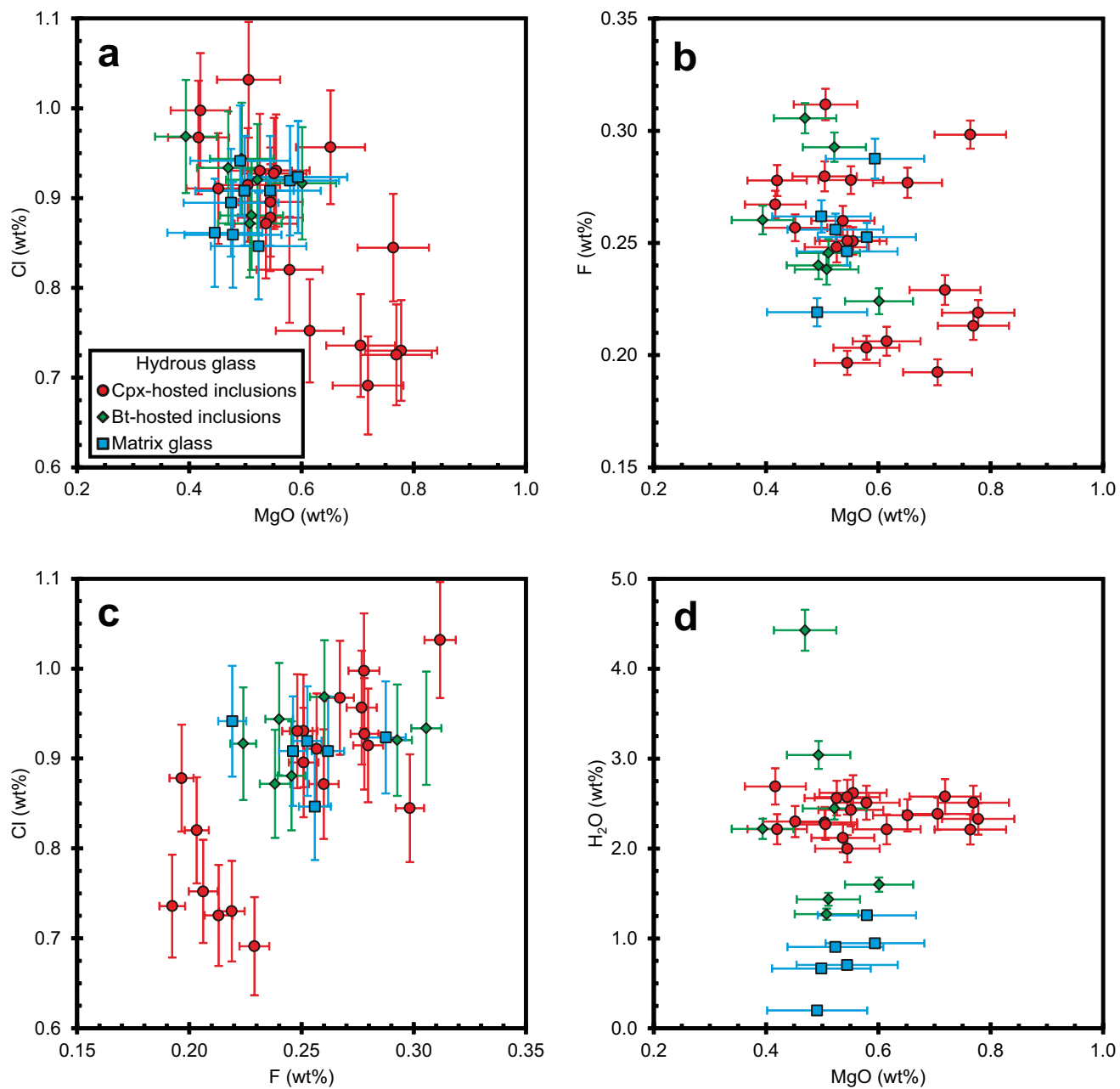


Figure 3

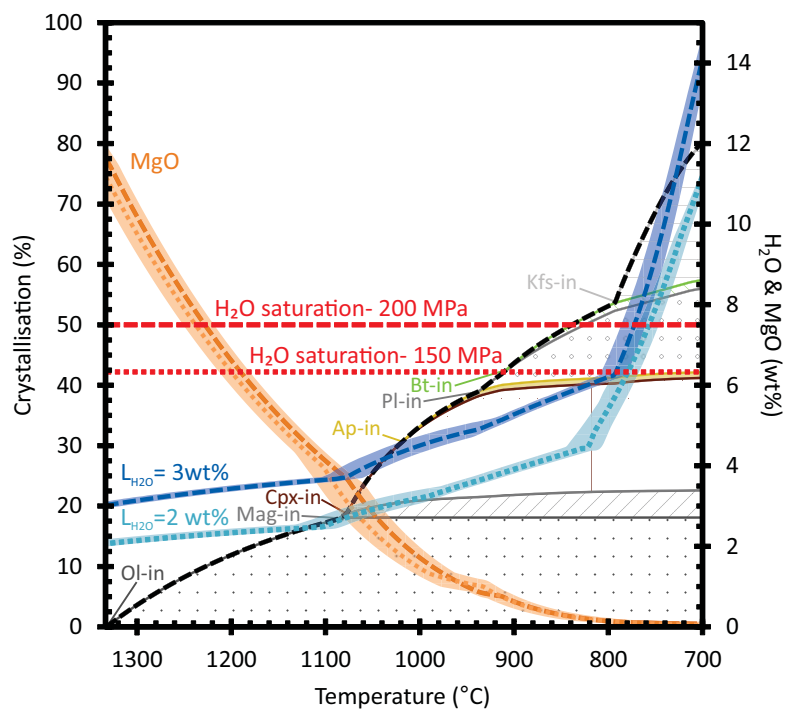


Figure 4